Progress in PHOTOVOLTAICS

PROGRESS IN PHOTOVOLTAICS: RESEARCH AND APPLICATIONS
Prog. Photovolt: Res. Appl. (2014)
Published online in Wiley Online Library (wileyonlinelibrary.com). DOI: 10.1002/pip.2565

APPLICATION

Subwavelength nanostructures integrated with polymer-packaged iii–v solar cells for omnidirectional, broad-spectrum improvement of photovoltaic performance

Xiaohan Li[1†], Ping-Chun Li[1†], Li Ji[1], Christopher Stender[2], Claiborne McPheeters[2], Sudersena Rao Tatavarti[2], Kimberly Sablon[3] and Edward T. Yu[1*]

[1] Microelectronics Research Center, The University of Texas at Austin, 10100 Burnet Road, Austin, TX 78758, USA
[2] Microlink Devices, Inc, 6457 West Howard St., Niles, IL 60714, USA
[3] U. S. Army Research Laboratory, 2800 Powder Mill Rd, Adelphi, MD 20783, USA

ABSTRACT

Reduction in surface and interface reflectance via the integration of subwavelength nanostructures in flexible polymer packaging material combined with incorporation of dielectric nanoislands into a conventional two-layer antireflection coating has been demonstrated, analyzed and optimized. Transmittance measurements of moth-eye textured polymer packaging sheets with different tapered pillar heights fabricated by reactive-ion etching and nanosphere lithography provide insights into the choice of the optimum nanostructure dimensions. Detailed computational modeling and simulations elucidate the physical nature of the antireflection performance of dielectric nanoisland structures integrated with a commercial two-layer antireflection coating, and provide guidance for design of the nanoisland structure for optimum antireflection performance. Measurements show that the integration of appropriately designed nanostructures in both polymer packaging material and conventional antireflection layers enables substantial increases in external quantum efficiency (E.Q.E.) and short-circuit current density (J_{sc}) over a broad range of incident angles, compared to structures with conventional bilayer antireflection coatings and unpatterned polymer packaging sheets. A 1.1× increase in J_{sc}, derived directly from E.Q.E. measurements, at normal incidence, increasing to 1.67× improvement at 80° angle of incidence, suggests that such an approach is promising for a variety of photovoltaic applications, particularly those where solar tracking is not feasible or practical. Copyright © 2014 John Wiley & Sons, Ltd.

KEYWORDS

antireflection; broad spectrum; omnidirectional; solar cells; subwavelength

***Correspondence**

Edward T. Yu, Electrical and Computer Engineering, The University of Texas at Austin, 10100 Burnet Road, Austin, TX 78758, USA.
E-mail: ety@ece.utexas.edu
[†]These authors contribute equally to this work.

Received 18 June 2014; Revised 25 August 2014; Accepted 17 September 2014

1. INTRODUCTION

III–V solar cells play a key role in photovoltaic energy harvesting for various space and terrestrial applications, and are leading candidates for concentrating photovoltaic and next-generation solar cell concepts [1–4]. Furthermore, recent advances in epitaxial growth and processing of III–V thin-film solar cells, including approaches for separation of active device layers from epitaxial growth substrates, have made III–V solar cells increasingly attractive for electricity generation strategies such as concentrated photovoltaic (CPV) systems [5] and mobile solar devices [6] that require very high energy conversion efficiency and/or reduced material usage [7–13]. However, in these photovoltaic applications, Fresnel reflection, particularly at large angles of incidence, becomes a major factor in limiting the overall energy conversion efficiency. Conventional planar thin-film antireflection coatings [14] are designed to provide excellent antireflection performance within limited ranges of angles of incidence and wavelengths. Furthermore, the limited number of materials with different refractive indices that exist in nature can constrain

improvements in the performance of such approaches, although nanostructured composite materials can provide a greater range of effective refractive indices [15–18].

Strategies based on subwavelength nanostructures, e.g. tapered moth-eye structures, that provide a graded-refractive index between air and the substrate to reduce Fresnel reflection in photovoltaic applications have been of considerable interest in recent years. They can be grouped into two categories based on their targeted materials: substrates of high and low refractive indices. Nanostructures fabricated on materials with high refractive indices such as Si or GaAs often require wet or dry etching of their substrates [19–22]. Although these structures can exhibit good broadband and omnidirectional antireflection performance, surface and near-surface material defects are typically introduced in etching processes, potentially resulting in reduced carrier collection efficiency, and in most cases an additional passivation layer is required to reduce photo-generated carrier recombination at these defects. On the other hand, subwavelength nanostructures on materials with low refractive indices are of great interest because of their wide usage as packaging materials in photovoltaic or display applications [23–28]. However, the fabrication of subwavelength nanostructures with sufficiently high aspect ratios and mechanical stability on materials with low refractive indices is still challenging.

Here we report the design, fabrication and optimization of a low-cost, large-area, multi-component, subwavelength antireflection structure that provides broadband, omnidirectional antireflection performance for a polymer-packaged GaAs single-junction solar cell. Two key elements are integrated within the final packaged structure—a moth-eye textured polyethylene terephthalate (PET) packaging sheet, and Al_2O_3 nanoislands on a single-junction GaAs solar cell with conventional Al_2O_3/TiO_2 bilayer antireflection coating. A rapid, large-area nanosphere lithography process [29–31] is employed to create both the moth-eye nanostructures on PET packaging sheets and Al_2O_3 nanoislands on Al_2O_3/TiO_2 antireflection coatings. Experimental studies of moth-eye nanostructures on PET reveal the optimal height of the nano-textured structure which provides the best transmittance performance over the entire wavelength range and incident angles ranging from 0° to 75°. Numerical simulations and experimental characterization of the Al_2O_3 nanoisland structures provide insights into the optimal periodicity and the physical origin of interference effects observed for the nanoisland structure. Finally, measurement results show that the integration of moth-eye textured PET packaging sheets together with Al_2O_3 nanoisland-coated GaAs single-junction solar cells leads to a significant increase in short-circuit current density (J_{sc}), as estimated from measured external quantum efficiency (E.Q.E.), ranging from 1.1× at normal incidence up to 1.67× at 80° of incidence compared to cells with conventional Al_2O_3/TiO_2 thin-film antireflection coating integrated with unpatterned PET packaging sheets.

2. EXPERIMENTAL SECTION

GaAs single junction solar cells were grow by metallorganic chemical vapor deposition (MOCVD) at 100 Torr using arsine (AsH_3), phosphine (PH_3), trimethylindium (TMI) and trimethylgallium (TMG) as precursors with a V/III ratio > 50. Single junction GaAs solar cells were grown on GaAs substrates. The growth structure consisted of InGaP window and back surface layer (BSF) layers, a 3.5-μm GaAs base layer with $2\times10^{17}\,cm^{-3}$ p-type doping and a 0.1-μm GaAs emitter with n-type doping in the range of $2\times10^{18}\,cm^{-3}$.

Numerical simulations were performed using the Rsoft Diffractmod software package (Rsoft Design Group, Inc., Ossining, NY, USA) and standard literature values for optical constants [32]. Incident light was assumed to be in the form of a plane wave impinging on the device surface. A simulated absorption spectrum was computed assuming optical absorption proportional to the square of the electric field amplitude, and the simulated E.Q.E. was computed assuming 100% efficiency in photo-generated carrier collection.

Optical transmittance measurements of moth-eye textured PET sheets were performed using collimated light from a halogen lamp spectrally resolved by a monochromator based system from Optronic Laboratories with AC lock in detection. The monochromatic light was linearly polarized by a Glan-Thompson polarizer before reaching the device. Devices were mounted on a rotating stage, allowing measurements to be performed at angles of 0° to 75° and at wavelengths ranging from 400 nm to 1100 nm. Photocurrent response spectra were measured at zero bias using the same monochromator system. The calculated J_{sc} for devices of each type under different incident angles was derived from E.Q.E. measurements weighted by the AM1.5G solar spectrum, given by Equation 1:

$$J_{sc} = e\int EQE(\lambda)I_{AM1.5}(\lambda)d\lambda \quad (1)$$

where e is the electron charge magnitude, and $I_{AM1.5}(\lambda)$ is the AM1.5G photon flux intensity.

Figure 1a shows schematic diagrams of the GaAs solar cell with a conventional Al_2O_3/TiO_2 bilayer antireflection coating integrated with Al_2O_3 nanoislands and moth-eye nanostructured PET packaging layer, together with the schematic refractive index profile. For the moth-eye nanostructures fabricated on the PET packaging sheet, NSL was employed in which 200-nm diameter polystyrene spheres were deposited in a hexagonal array as a soft mask using a Langmuir-Blodgett process [29,33,34] as shown in Figure 1b. Subsequent reactive-ion etching creates the moth-eye nanostructure on the PET surface, consisting of arrays of tapered cylindrical pillars of height ~ 400 nm as shown in Figure 1c–d. Figure 1e shows a scanning electron micrograph (SEM) image of the completed moth-eye structure on a PET surface. Similarly, for the nanoisland structure fabricated directly on the cell surface, NSL was

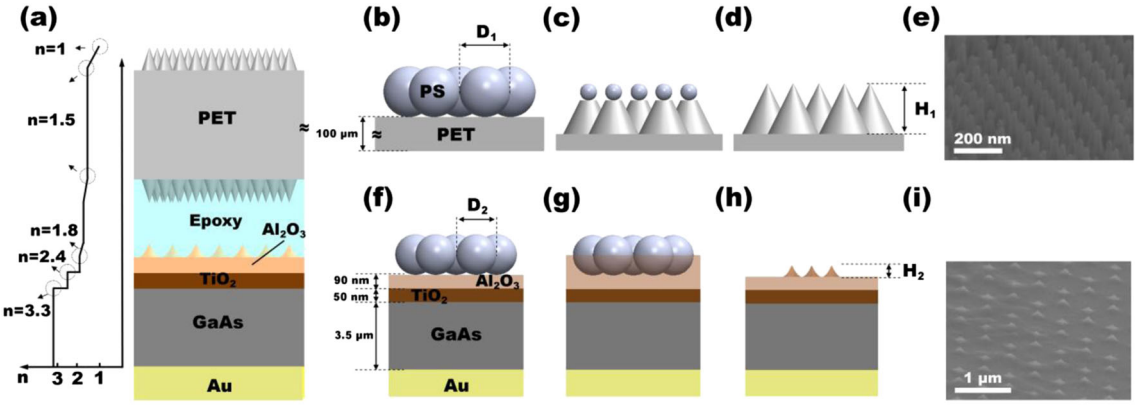

Figure 1. a) Schematic diagram of a polymer-packaged GaAs solar cell coated with conventional Al_2O_3/TiO_2 bilayer antireflection coating with Al_2O_3 nanoislands and integrated with double-side moth-eye textured PET packaging sheet by space-grade encapsulant, together with the vertical refractive index profile. b)–d) Schematic diagrams of process flow for fabricating moth-eye structure on PET substrate. e) SEM image of the completed moth-eye structure on PET substrate. f)–h) Schematic diagram of process flow for fabricating Al_2O_3 nanoislands structure on Al_2O_3/TiO_2 bilayer antireflection coating. i) SEM image of the completed nanoislands structure.

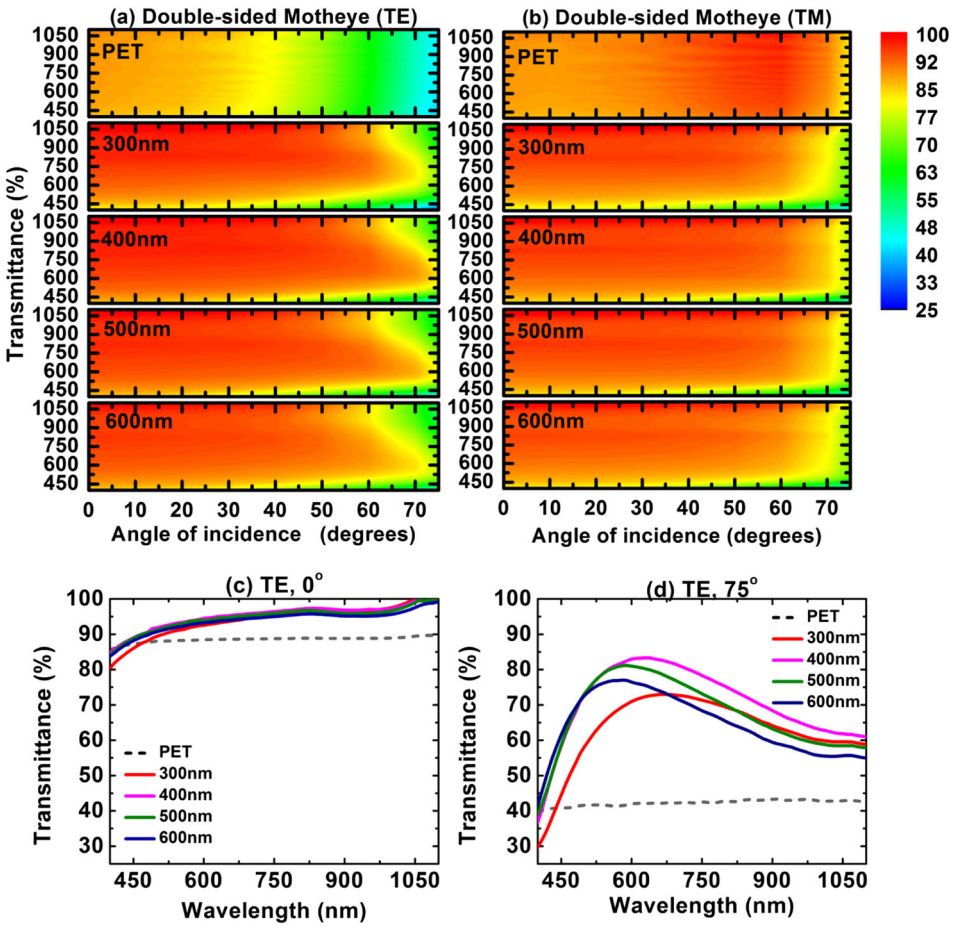

Figure 2. a), b) Transmittance measurements for planar and double-side moth-eye textured PET packaging sheet of various texturing depths with TE/TM-polarized incident light. The measurements were performed for wavelengths ranging from 400 nm to 1100 nm, with incident angles varying from 0° to 75°. c), d) Transmittance measurements for unpatterned and double-side moth-eye textured PET packaging sheet of various etching time at 0° and 75° incident angle under TE-polarized illumination, respectively.

employed in which 1000-nm diameter polystyrene spheres were deposited as shown in Figure 1f. Al_2O_3 (500 nm) was then deposited by e-beam evaporation (Figure 1g), followed by a lift-off process to remove the polystyrene spheres (Figure 1h), resulting in a hexagonal array of Al_2O_3 nanoislands of height ~150 nm. An SEM image of the completed nanoisland structure is shown in Figure 1i. The PET packaging sheet is attached to the cell substrate using a space-grade encapsulant (Dow Corning 93-500).

3. RESULTS AND DISCUSSION

Figure 2a shows the optical transmittance measured as a function of angle of incidence and wavelength for an unpatterned PET sheet and for a double-side moth-eye textured PET sheet with $D_1 = 200$ nm, and with different heights, H_1, of 300 nm to 600 nm under TE-polarized illumination. All moth-eye textured PET sheets show significantly improved transmittance characteristics compared to that of the unpatterned PET sheet at wavelengths ranging from 400 nm to 1100 nm and at incident angles from 0° to 75°. Similar transmittance measurements were carried out with the same set of structures of each type with TM-polarized incident light as shown in Figure 2b. In these cases, the planar PET sheet shows slightly lower transmittance compared to moth-eye textured PET sheets at incident angles $< 60°$, and slightly higher transmittance at incident angles $> 60°$. In principle, an optimal graded-refractive index structure will yield the best performance [35–38]; however, the optimal structures often require large ratios of height to diameter to assure a sufficiently smooth, gradual change in refractive index, [28] which is extremely challenging in terms of fabrication. We therefore compare the transmittance characteristics of these moth-eye structures within a physically attainable range of heights. Figure 2c shows the comparison of measured transmittance characteristics for unpatterned and double-side moth-eye textured nanostructures on PET sheets with different H_1 at 0°. All moth-eye structures show ~5% improvement in transmittance compared with unpatterned PET sheet. Figure 2d shows the measured transmittance of double side moth-eye textured nanostructures with different H_1 at 75° incident angle. Within these structures, $H_1 = 400$ nm shows the best performance, with ~40% (~2×) enhancement in transmittance compared to that of the unpatterned PET substrate at 600-nm wavelength. The transmittance spectra of structures with $H_1 = 300$, 500 and 600 nm also show enhancement, but of less magnitude than that of the structure with $H_1 = 400$ nm, suggesting that the antireflection performance saturates at a certain height of the moth-eye nanostructure.

The moth-eye patterns fabricated in the PET sheets provide a gradual transition in refractive index from air to the PET packaging material. Additional measures are required to reduce reflectance at the interface between the epoxy

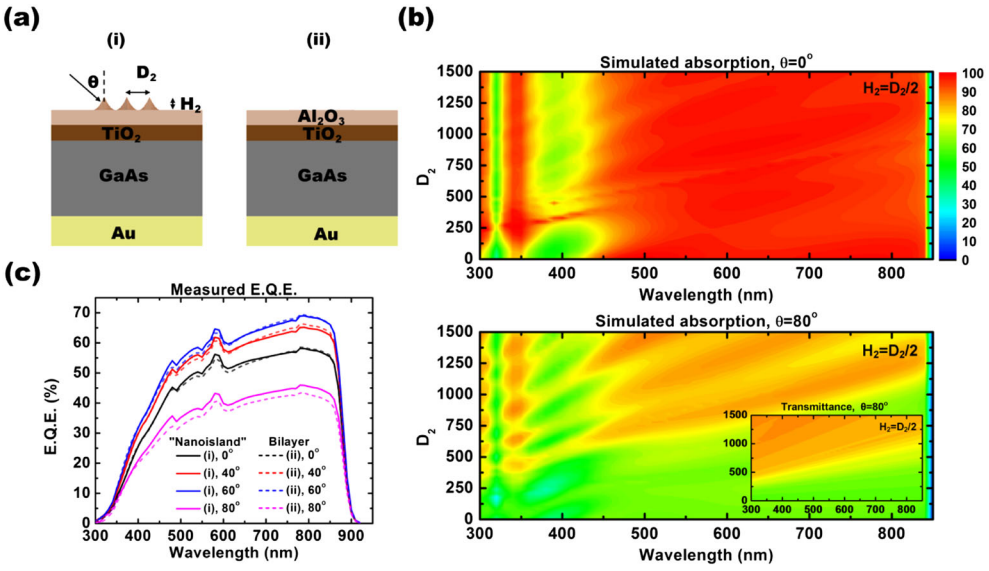

Figure 3. a) Schematic diagrams of GaAs solar cells coated with conventional Al_2O_3/TiO_2 bilayer antireflection coating with and without Al_2O_3 nanoislands structure. b) (Top) Simulated cell absorption at normal incidence for incident wavelengths from 300 nm to 850 nm with the nanosphere diameter D_2 ranging from 0 nm to 1500 nm while keeping the height of the nanoislands $H_2 = D_2/2$. (Bottom) Simulated cell absorption at 80° incidence for incident wavelengths from 300 nm to 850 nm with the nanosphere diameter D_2 varying from 0 nm to 1500 nm while keeping the height of the nanoislands $H_2 = D_2/2$. (Inset) Simulated transmittance of Al_2O_3 nanoislands structure at 80° incidence for incident wavelengths from 300 nm to 850 nm with the nanosphere diameter, D_2 varying from 0 nm to 1500 nm while keeping the height of the nanoislands $H_2 = D_2/2$. The incident light was polarized as 45° in order to include the same amount of TE and TM polarizations simultaneously. c) E.Q.E. measurements for GaAs cells with and without Al_2O_3 nanoislands. The measurements were performed for wavelengths ranging from 300 nm to 920 nm, with incident angles varying from 0° to 80°.

and the Al_2O_3 thin-film antireflection layers. We employ Al_2O_3 nanoislands for this purpose, examining first the effects of the nanoisland structure without PET packaging sheets. Figure 3a shows schematic diagrams of the GaAs single-junction solar cell deposited with conventional Al_2O_3/TiO_2 thin-film bilayer antireflection coating with (i) and without (ii) the additional Al_2O_3 nanoisland structure [30,31]. Figure 3b shows the numerically simulated absorption of structure (i) as a function of wavelength and periodicity (D_2) for $\theta = 0°$ and 80°. The height of the Al_2O_3 nanoislands, H_2, is assumed to be $D_2/2$ for an ideal structure. For $\theta = 0°$, we observe that the overall absorption remains close to 100%, except for two minima from 310 nm to 330 nm and 370 nm to 420 nm that are present for all values of D_2. These absorption dips result from Fabry–Perot interference associated with the underlying Al_2O_3/TiO_2 bilayer antireflection coating, and they play a less significant role in the cell's photovoltaic performance since the E.Q.E. of the GaAs cell at these wavelengths is low. The overall antireflection performance of the Al_2O_3 nanoisland structure is similar to that of a standard bilayer antireflection coating since the antireflection performance of the bilayer structure is optimized at smaller angles of incidence.

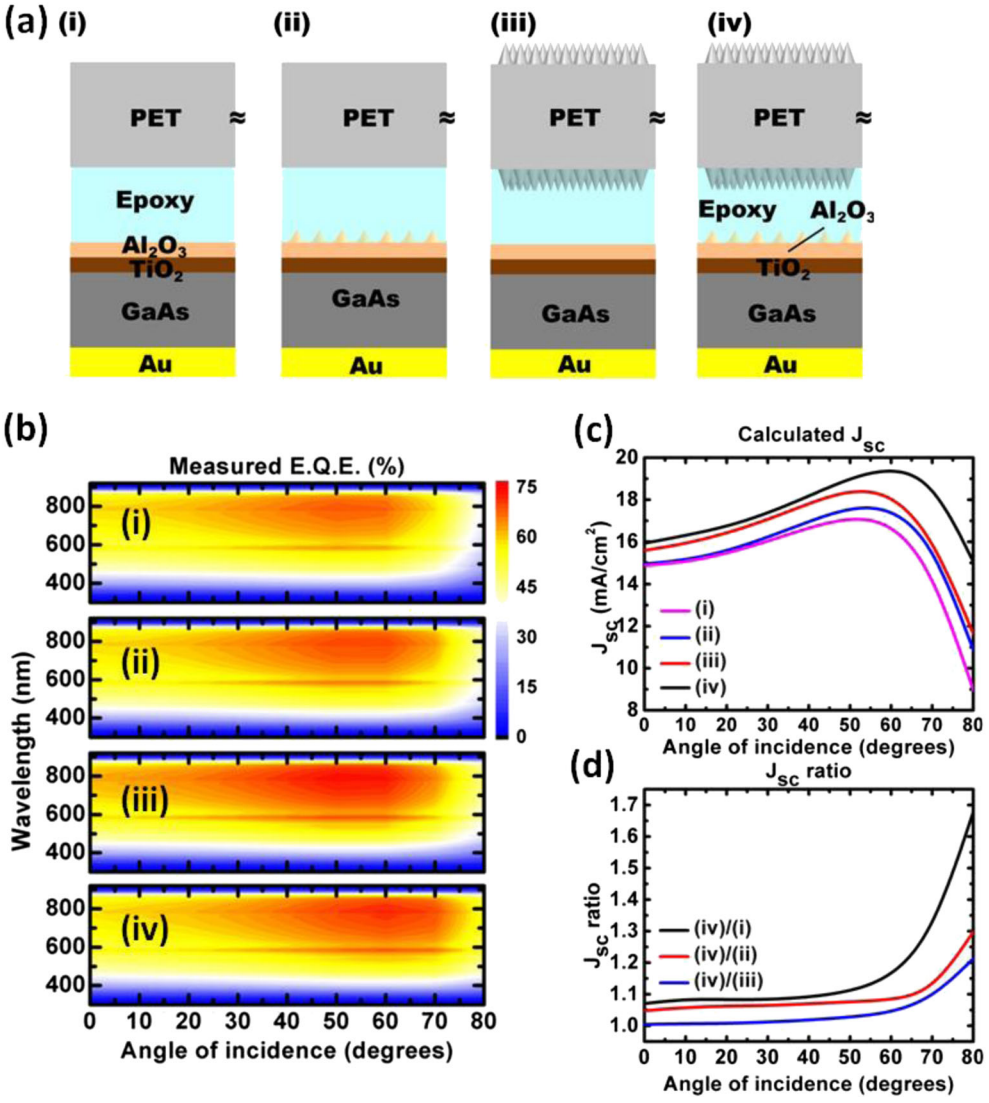

Figure 4. a) Schematic diagrams of various integrated structures under comparison: (i) GaAs solar cell without Al_2O_3 nanoislands integrated with unpatterned PET packaging sheet; (ii) GaAs solar cell with Al_2O_3 nanoislands integrated with unpatterned PET packaging sheet; (iii) GaAs solar cell without Al_2O_3 nanoislands integrated with moth-eye patterned PET packaging sheet and (iv) GaAs solar cell with Al_2O_3 nanoislands integrated with moth-eye patterned PET packaging sheet. b) E.Q.E. measurements for devices of each configuration at wavelengths from 300 nm to 920 nm, with incident angles varying from 0° to 80°. c) Calculated J_{sc} for devices of each configuration, derived from E.Q.E. measurements weighted by AM1.5G solar spectrum. d) Calculated ratio for J_{sc} of integrated device (iv) over that of integrated structures (i), (ii) and (iii) with varying incident angles from 0° to 80°.

For $\theta = 80°$, the influence of the Al_2O_3 nanoisland structure becomes more prominent. The maximum absorption is observed for $D_2 > 500$ nm due to the enhanced transmittance from the graded-index profile of Al_2O_3 nanoislands. In addition to absorption dips (from 310 nm to 330 nm and 370 nm to 420 nm) resulting from the interference of the bilayer antireflection coating, we observe straight interference lines in the simulated contour map. Similar interference lines are observed in the numerically simulated transmittance for Al_2O_3 nanoislands on bulk Al_2O_3 (as shown in the inset) for $\theta = 80°$, with interference line positions very close to those observed in the simulated absorption of structure (i) for $\theta = 80°$. These observations reveal that the physical origin of the interference at $\theta = 80°$ is from the Fabry–Perot resonances of the Al_2O_3 nanoisland structure at certain combinations of height and wavelength. From these simulations, we conclude that for optimized antireflection performance at large incident angles, the diameter/height of the Al_2O_3 nanoisland structure can be chosen in the range $500\,\text{nm} < D_2 < 1200\,\text{nm}$, since even taller nanoisland structures can only provide a limited degree of improvement, but can be more challenging in terms of fabrication. Figure 3c shows the measured E.Q.E. of structure (i) with $D_2 = 1000$ nm (solid lines), and structure (ii) (dashed lines) at different θ. For $\theta = 0°$ to 60°, the measured E.Q.E. of structures (i) and (ii) are similar because the bilayer antireflection coating can provide reasonably good performance for $\theta < 60°$. For $\theta = 80°$, the measured E.Q.E. of structure (ii) is higher than that of (i) but with less significant enhancement compared with simulated results due to limitations on the values of H_2 that can be achieved in the fabrication process.

Figure 4a shows schematic diagrams of the full set of different integrated structures we compare experimentally, including (i) GaAs cell without Al_2O_3 nanoislands integrated with unpatterned PET packaging sheet; (ii) GaAs cell with Al_2O_3 nanoislands integrated with unpatterned PET packaging sheet; (iii) double-side moth-eye textured PET packaging sheet integrated with GaAs cell with conventional Al_2O_3/TiO_2 bilayer antireflection coating; and (iv) the double-side moth-eye textured PET packaging sheet integrated with GaAs single-junction solar cell with the Al_2O_3 nanoisland structure. Measured E.Q.E. of devices of each type under incident angles from 0° to 80° is shown in Figure 4b. Substantially enhanced E.Q.E. can be observed for structures (ii), (iii) and (iv), particularly at large incident angles (incident angles $> 70°$), compared to the unpatterned cell (i).

Figure 4c shows the calculated normalized J_{sc} for devices of each configuration under different incident angles, derived from E.Q.E. measurements weighted by the AM1.5G solar spectrum. Note that, in this plot, the illumination intensity does not vary with incident angle, so that the "cosine law" decrease in current density does not occur. This allows the influence of the PET moth-eye and Al_2O_3 nanoisland structures on optical reflectance to be more easily observed. First, we observe that configuration (ii), compared with the unpatterned cell (i), shows very similar J_{sc} values at small incident angles and improved J_{sc} values particularly at large incident angles, which is consistent with our numerical simulation results as shown in Figure 4c. Further inspection shows that a significant improvement in J_{sc} is obtained with structure (ii) compared to structure (i) at large incident angles, due to the graded transition in refractive index at the epoxy–Al_2O_3 interface that is achieved. Next, we compare structure (iii) with structures (ii) and (i), and observe improved J_{sc} over the entire range of incident angles (0°–80°) due to the moth-eye nanostructured PET packaging sheet surface, which significantly reduces interface reflectance between air and the polymer packaging layer. Finally, we observe that structure (iv) with both types of integrated nanostructures shows even larger improvement in J_{sc} compared to other structures over the entire range of incident angles, which demonstrates the superior photovoltaic performance of our integrated optical nanostructures that effectively reduce reflectance at all the key interfaces in the fully packaged structure via optimization of the refractive index profile. Figure 4d shows the calculated ratio of the J_{sc} of the cell with both Al_2O_3 nanoislands and moth-eye textured PET packaging sheet over cells with other configurations. A 1.1° increase in J_{sc} at normal incidence, increasing to 1.67° at 80° angle of incidence, was achieved by the nanostructured cell (iv) compared to the cell without optical nanostructures (i), which shows the great promise for this approach in boosting the energy conversion efficiency over a wide range of incident angles for various photovoltaic systems.

4. CONCLUSION

We have demonstrated and analyzed a broadband, omnidirectional antireflection approach for solar cells integrated with polymer packaging based on creating moth-eye textures on polymer (PET) packaging sheets combined with Al_2O_3 nanoisland structures, which shows significant enhancement in calculated J_{sc} values derived from E.Q.E. measurements under normal and off-normal incident conditions compared to the conventional cell without optical nanostructures, using a low-cost, high-throughput NSL process. Transmittance measurements of moth-eye patterned PET packaging sheets with nanosphere periods of 200 nm and with different tapered pillar heights show that the nano-patterned PET sheet with pillar heights of 400 nm provides the optimum transmittance characteristics, maintaining >90% transmittance within wavelengths from 400 nm to 1050 nm under normal incidence and >70% transmittance within wavelengths from 500 nm to 900 nm at an incident angle of 80°. Detailed numerical simulations provide insights into the choice of dimensions for Al_2O_3 nanoislands, which are in good agreement with experimental measurement results. Finally, E.Q.E. measurements of the cell with Al_2O_3 nanoislands integrated with a moth-eye textured PET packaging sheet and control cells with different antireflection configurations were

performed. The combination of these approaches yields ~10% increase in J_{sc} at normal incidence and up to ~67% increase at an incident angle of 80° compared to the control cell without optical nanostructures, based on measurements of E.Q.E. combined with the AM1.5G solar spectrum. We conclude that such an approach is an economical, viable and highly promising antireflection strategy for various photovoltaic applications, particularly for those in concentrated PV and mobile solar systems where sufficiently high energy harvesting efficiency over a broadband of wavelengths and a wide range of incident angles is particularly desirable.

ACKNOWLEDGEMENTS

Part of this work was supported by the U. S. Army Research Laboratory, the National Science Foundation (ECCS-1120832 and DMR-1311866) and the Judson S. Swearingen Regents Chair in Engineering at the University of Texas at Austin. P.-C. Li would like to thank H.-H. Kung (Rutgers University) and E.-S. Liu (UT-Austin) for fruitful discussions on nanosphere lithography. X. H. Li and P. –C. Li contributed equally to this work.

REFERENCES

1. Ekins-Daukes NJ, Barnham KWJ, Connolly JP, Roberts JS, Clark JC, Hill G, Mazzer M. Stain balanced GaAsP/InGaAs quantum well solar cells. *Applied Physics Letters* 1999; **75**: 4195–4197.
2. Luque A, Marti A, Stanley C. Understanding intermediate-band solar cells. *Nature Photonics* 2012; **6**: 146–152.
3. Sablon KA, Little JW, Mitin V, Sergeev A, Vagidov N, Reinhardt K. Strong enhancement of solar cell efficiency due to quantum dots with built-in charge. *Nano Letters* 2011; **11**: 2311–2317.
4. Cotal H, Fetzer C, Boisvert J, Kinsey G, King R, Hebert P, Yoon H, Karam N. III/V multijunction solar cells for concentrating photovoltaics. *Energy & Environmental Science* 2009; **2**: 174–192.
5. Winston R, Minano JC, Benitez P. *Nonimaging Optics*. Elsevier Academic Press: Burlington, MA, USA, 2005.
6. Trautz KM, Jenkins PP, Walters RJ, Scheiman D, Hoheisel R, Tatavarti R, Chan R, Miyamoto H, Adams JGJ, Elarde VC, Grimsley J. Mobile Solar Power. *IEEE Journal of Photovoltaics* 2013; **3**(1): 535–541.
7. Yoon J, Jo S, Chun IS, Jung I, Kim HS, Meitl M, Menard E, Li X, Coleman JJ, Paik U, Rogers JA. GaAs photovoltaics and optoelectronics using reusable multilayer epitaxial assemblies. *Nature* 2010; **465**: 329–333.
8. Yu P, Chiu MY, Chang CH, Hong CY, Tsai YL, Han HV, Wu YR. Towards high-efficiency multi-junction solar cells with biologically inspired nanosurfaces. *Progress in Photovoltaics: Research and Applications* 2014; **22**: 300–307.
9. Guter W, Schöne J, Philipps SP, Steiner M, Siefer G, Wekkeli A, Welser E, Oliva E, Bett AW, Dimroth F. Current-matched triple-junction solar cell reaching 41.1% conversion efficiency under concentrated sunlight. *Applied Physics Letters* 2009; **94**: 223504.
10. Wei G, Shiu KT, Giebink NC, Forrest SR. Thermodynamic of quantum photovoltaic cell efficiency. *Applied Physics Letters* 2007; **91**: 223507.
11. Konagai M, Sugimoto M, Takahashi K. High efficiency GaAs thin film solar cells by peeled film technology. *Journal of Crystal Growth* 1978; **45**: 277–280.
12. Bauhuis GJ, Mulder P, Haverkamp EJ, Huijben JCCM, Schermer JJ. 26.1% thin-film GaAs solar cell using epitaxial lift-off. *Solar Energy Materials and Solar Cells* 2009; **93**: 1488–1491.
13. Liang D, Huo Y, Kang Y, Wang KX, Gu A, Tan M, Yu Z, Li S, Jia J, Bao X, Wang S, Yao Y, Wong HSP, Fan S, Cui Y, Harris JS. Optical absorption enhancement in freestanding GaAs thin film nanopyramid arrays. *Advanced Energy Materials* 2012; **2**: 1254–1260.
14. Macleod HA. *Thin-Film Optical Filters*. CRC Press: New York, 2010.
15. Xi JQ, Schubert MF, Kim JK, Schubert EF, Chen M, Lin SY, Liu W, Smart JA. Optical thin-film materials with low refractive index for broadband elimination of Fresnel reflection. *Nature Photonics* 2007; **1**: 176–179.
16. Schubert MF, Mont FW, Chhajed S, Poxson DJ, Kim JK, Schubert EF. Design of multilayer antireflection coatings made from co-sputtered and low-refractive-index materials by genetic algorithm. *Optics Express* 2008; **16**: 5290–5298.
17. Chhajed S, Schubert MF, Kim JK, Schubert EF. Nanostructured multilayer graded-index antireflection coating for Si solar cells with broadband and omnidirectional characteristics. *Applied Physics Letters* 2008; **93**: 251108.
18. Yan X, Poxson DJ, Cho J, Welser RE, Sood AK, Kim JK, Schubert EF. Enhanced omnidirectional photovoltaic performance of solar cells using multiple-discrete-layer tailored-and low-refractive index anti-reflection coatings. *Advanced Functional Materials* 2013; **23**: 583–590.
19. Park H, Shin D, Kang G, Baek S, Kim K, Padilla WJ. Broadband optical antireflection enhancement by integrating antireflective nanoislands with silicon nanoconical-frustum arrays. *Advanced Materials* 2011; **23**: 5796–5800.

20. Chen JY, Yu MH, Chang SF, Sun KW. Highly efficient poly (3,4-ethylenedioxythiophene): poly (styrenesulfonate)/Si hybrid solar cells with imprinted nanopyramid structures. *Applied Physics Letters* 2013; **103**: 133901.
21. Huang YF, Chattopadhyay S, Jen YJ, Peng CY, Liu TA, Hsu YK, Pan CL, Lo HC, Hsu CH, Chang YH, Lee CS, Chen KH, Chen LC. Improved broadband and quasi-omnidirectional anti-reflection properties with biomimetic silicon nanostructures. *Nature Nanotechnology* 2007; **2**: 770–774.
22. Sun CH, Ho BJ, Jiang B, Jiang P. Biomimetic subwavelength antireflective gratings on GaAs. *Optics Letters* 2008; **33**: 2224–2226.
23. Choi K, Park SH, Song YM, Lee YT, Hwangbo CK, Yang H, Lee HS. Nano-tailoring the surfacestructure for the monolithic high-performance antireflection polymer film. *Advanced Materials* 2010; **22**: 3713–3718.
24. Park KC, Choi HJ, Chang CH, Cohen RE, McKinley GH, Barbastathis G. Nanotextured silica surfaces with robust superhydrophobicity and omnidirectional broadband supertransmissivity. *ACS Nano* 2012; **6**: 3789–3799.
25. Yamada N, Ijiro T, Okamoto E, Hayashi K, Masuda H. Characterization of antireflection moth-eye film on crystalline silicon photovoltaic module. *Optics Express* 2011; **19**: A118–A125.
26. Son J, Sakhuja M, Danner AJ, Bhatia CS, Yang H. Large scale antireflective glass texturing using grid contacts in anodization methods. *Solar Energy Materials and Solar Cells* 2013; **116**: 9–13.
27. Sakhuja M, Son J, Verma LK, Yang H, Bhatia CS, Danner AJ. Omnidirectional study of nanostructured glass packaging for solar modules. *Progress in Photovoltaics: Research and Applications* 2014; **22**: 356–361.
28. Li PC, Yu ET. Large-area omnidirectional coating on low-index materials. *Journal of the Optical Society of America B* 2013; **30**: 2584–2588.
29. Rybczynski J, Ebels U, Giersig M. Large-scale, 2D arrays of magnetic nanoparticles. *Colloids and Surfaces A: Physicochemical and Engineering Aspects* 2003; **219**: 1–6.
30. Li XH, Li PC, Hu DZ, Schaadt DM, Yu ET. Light trapping in thin-film solar cells via scattering by nanostructured antireflection coatings. *Journal of Applied Physics* 2013; **114**: 044310.
31. Li XH, Li PC, Hu DZ, Schaadt DM, Yu ET. Angular dependence of light trapping in $In_{0.3}Ga_{0.7}As$/GaAs quantum-well solar cells. *Journal of Applied Physics* 2014; **115**: 044303.
32. Palik ED. *Handbook of Optical Constants of Solids*. Academic Press: New York, 1998.
33. Ho CC, Chen PY, Lin KH, Juan WT, Lee WL. Fabrication of monolayer of polymer/nanospheres hybrid at a water-air interface. *ACS Applied Materials & Interfaces* 2011; **3**: 204–208.
34. Li PC, Yu ET. Flexible, low-loss, large-area, wide-angle, wavelength-selective plasmonic multilayer metasurface. *Journal of Applied Physics* 2013; **114**: 133104.
35. Chen M, Chang HC, Chang ASP, Lin SY, Xi JQ, Schubert EF. Design of optical path for wide-angle graded-index antireflection coatings. *Applied Optics* 2007; **46**: 6533–6538.
36. Raguin DH, Morris GM. Antireflection structured surfaces for the infrared spectral region. *Applied Optics* 1993; **32**: 1154–1167.
37. Grann EB, Moharam MG, Pommet DA. Artificial uniaxial and biaxial dielectrics with use of two-dimensional subwavelength binary gratings. *Journal of the Optical Society of America A* 1994; **11**: 2695–2703.
38. Grann EB, Varga MG, Pommet DA. Optimal design for antireflective tapered two-dimentional subwavelength grating structures. *Journal of the Optical Society of America A* 1995; **12**: 333–339.